Reducing spin-up time for simulations of turbulent channel flow

K. S. Nelson, and O. B. Fringer

Citation: Physics of Fluids **29**, 105101 (2017); doi: 10.1063/1.4993489
View online: http://dx.doi.org/10.1063/1.4993489
View Table of Contents: http://aip.scitation.org/toc/phf/29/10
Published by the American Institute of Physics

Reducing spin-up time for simulations of turbulent channel flow

K. S. Nelson[a] and O. B. Fringer
The Bob and Norma Street Environmental Fluid Mechanics Laboratory, Stanford University, Stanford, California 94305, USA

(Received 29 June 2017; accepted 13 September 2017; published online 4 October 2017)

Spin-up of turbulent channel flow forced with a constant mean pressure gradient is prolonged because the flow accelerates due to an imbalance between the driving pressure gradient and total bottom stress. To this end, a method ensuring a time invariant volume-averaged streamwise velocity during spin-up is presented and compared to simulations forced with a mean pressure gradient for both linear and logarithmic initial velocity profiles. The comparisons are made for open-channel flow with a friction Reynolds number Re_τ of 500. Additional simulations with Re_τ ranging from 1 to 400 are also run to confirm validity of the method for a range of Reynolds numbers. While the method eliminates spin-up time related to approaching the target volume-averaged velocity, spin-up time is still required for the flow to transition to turbulence and reach statistical equilibrium. Therefore, the time evolution of turbulence in response to different initial velocity profiles and random perturbations is investigated. Simulations initialized with linear velocity profiles trigger turbulence and reach statistical equilibrium sooner than those initialized with logarithmic profiles given the same initial perturbations, a manifestation of the increased shear created by linear profiles. The results suggest that, combined with appropriate initial conditions, ensuring a time invariant volume-averaged streamwise velocity can reduce the computational time associated with spin-up of turbulent open-channel flows by at least a factor of five. *Published by AIP Publishing.* https://doi.org/10.1063/1.4993489

I. INTRODUCTION

The geometric simplicity and ubiquitous nature of turbulent channel flow have inspired numerical investigations for decades. By applying large-eddy simulation (LES), Deardorff[1] and Schumann[2] were among the first to numerically simulate wall-bounded turbulence. These pioneering investigations did not resolve the viscous wall region, a challenge overcome by Moin and Kim[3] and later with higher fidelity by Kim *et al.*,[4] the latter applying direct numerical simulation (DNS). Since then, computing advancements have enabled resolved turbulent channel flow simulations with ever increasing Reynolds numbers,[5–10] domain complexities,[11–13] and stratification effects.[14–16]

Despite tremendous improvements in computing abilities, the primary challenge of simulating turbulent channel flow is the required computational expense. Millions of central processing unit (CPU) hours are needed to simulate even modest Reynolds number flows. For example, 6×10^6 CPU hours were used by Hoyas and Jiménez[7] to simulate channel flow with a friction Reynolds number of 2003. Computational resources are expended not only in data collection for flow analyses but also during spin-up when flow evolves from initial conditions to statistical equilibrium.

Spin-up time is often minimized by initializing simulations with a turbulent dataset expected to be statistically similar to the target flow conditions. Literature review reveals progression of simulations in which final conditions of one study become the initial conditions of the next. For example, the initial conditions used by Kim *et al.*[4] were obtained from Moin and Kim,[3] who initialized their simulations from a dataset passed on by Kim and Moin.[17] Even with a starting dataset, a series of grid refinement simulations is sometimes required.[18] Furthermore, accurate interpolation of an initial three-dimensional turbulent flow field can be challenging, particularly in complex geometries.

If a dataset for initialization is unavailable, channel flow simulations are typically initialized with a parabolic Poiseuille or log-law mean velocity profile plus random perturbations to trigger turbulence. Simulations are then time advanced by driving the flow with a mean pressure gradient until the flow becomes statistically steady. The assigned driving pressure gradient can be constant[16,19] or time dependent[3–5,20] if a constant bulk, or volume-averaged, velocity ($\overline{u}$) is desired. Forcing simulations with a constant pressure gradient is numerically simple to implement as the driving pressure gradient required for a given Reynolds number is known *a priori* for statistically steady flow. However, during spin-up, the pressure gradient typically is not balanced by the total bottom stress. This imbalance leads to flow acceleration beyond the target mean velocity, prolonging the time to reach statistical equilibrium. As will be shown in Sec. III A, the overshoot is avoided if the driving pressure force is exactly balanced by the bottom stress.

Since turbulent channel flow is uniquely characterized by the volume-averaged velocity, the channel height (H), and the kinematic viscosity (ν), the Buckingham Pi theorem implies that only one nondimensional parameter characterizes the flow; in this case, the bulk Reynolds number $Re_b = \overline{u}H/\nu$. Alternatively, if instead we use the friction velocity (u_*), then the problem is characterized by the friction Reynolds number $Re_\tau = u_* H/\nu$. We note that only one of u_* or $\overline{u}$ can be specified

[a]Electronic mail: knelson3@stanford.edu

since u_* and $\overline{u}$ are not independent. Regardless, if $\overline{u}$ is held constant during a simulation, then the problem is completely specified by initializing the flow with the desired volume-averaged velocity. Holding $\overline{u}$ constant, however, requires dynamically adjusting the driving pressure gradient as simulations evolve.

Numerous studies have implemented methods for maintaining a constant volume-averaged velocity. However, derivations of the methods and implementation strategies are commonly omitted from the literature.[3–5,20] Moreover, many methods employ *ad hoc* coefficients,[21,22] do not exactly guarantee a constant volume-averaged velocity,[22,23] or unnecessarily require a depth-dependent correction to the velocity field[24] that is only applicable for simple rectangular domains. To the best of our knowledge, the reduction in time associated with constant volume-averaged velocity approaches also has not been directly compared to the constant pressure gradient method in the literature.

In this paper, we derive (Sec. II B) and outline the implementation (Sec. II C) of a method that exactly enforces a constant volume-averaged velocity or flow rate as bottom stresses evolve from a laminar to turbulent state for turbulent channel or open-channel flow. We also explicitly show that the method significantly reduces the computational time required to achieve statistically steady turbulence (Sec. III A). We present the method as applied to a finite-volume framework in a curvilinear coordinate system, following Zang *et al.*,[25] in a simple rectangular domain. The method can, however, be implemented within spectral solvers and can be applied to any domain shape (for example, with open-channel flow over bed forms). The method also does not require cumbersome interpolation of a flow field that was precomputed on a different grid. In Sec. III D, we investigate differences between simulations initialized with linear and log-law mean velocity profiles with varying magnitudes of the initial perturbations to assess the effects of initial conditions on the time required to transition to turbulent flow.

II. NUMERICAL IMPLEMENTATION

A. Terminology and notation

In the derivation and analysis that follows, we adopt the notation of Chou and Fringer.[19] For an arbitrary variable ϕ^n, we represent discrete volume-averaging with an overbar ($\overline{\phi}^n$), planform averaging with a tilde ($\widetilde{\phi}^n$), and time-averaging with angle brackets ($\langle\phi^n\rangle$), each defined as

$$\overline{\phi}^n = \frac{1}{V}\sum_x\sum_y\sum_z \phi^n \Delta x\Delta y\Delta z, \tag{1}$$

$$\widetilde{\phi}^n = \frac{1}{A}\sum_x\sum_y \phi^n \Delta x\Delta y, \tag{2}$$

and

$$\langle\phi^n\rangle_N = \frac{1}{N}\sum_{j=n-N+1}^{n} \phi^j, \tag{3}$$

where V is the domain volume, A is the planform area of the domain, and N is the number of time steps over which time averaging is performed. Here, x, y, and z are taken as the streamwise, spanwise, and vertical directions, respectively, and the superscripts indicate the time step. Velocity fluctuations are defined as deviations from the planform average with $u_i' = u_i - \widetilde{u_i}$. Finally, a superscript plus ($^+$) implies nondimensionalization of length by the viscous length scale ν/u_* and velocity by the friction velocity u_*.

In contrast to traditional channel flow simulations in which the top and bottom boundaries employ no-slip conditions ($u = v = w = 0$), we implement open-channel flow simulations with a free-slip top boundary condition ($\partial_z u = \partial_z v = 0$ and $w = 0$). Such a boundary condition is employed because we focus on environmental flow problems which represent the free surface with a free-slip, rigid-lid at the top boundary. Although our focus is on open-channel flows, the method can be applied to traditional channel flow simulations without any modifications other than changing the boundary conditions.

B. Numerical method

We begin by writing the streamwise momentum (u-velocity component) update equation as a two-step method with the addition of a forcing function, S, that varies in time but is constant in space, viz.,

$$\widehat{u} = u^n + \Delta t R^{n+\frac{1}{2}}, \tag{4}$$

$$u^{n+1} = \widehat{u} + \Delta t S^{n+\frac{1}{2}}. \tag{5}$$

The splitting of Eqs. (4) and (5) is performed to illustrate that the method is implemented in two primary steps and as a conceptual tool in the method derivation. However it is not related to pressure projection methods commonly used to simulate incompressible flows because the added forcing function is spatially constant and so does not alter the divergence. On the right-hand side of Eq. (4), $R^{n+\frac{1}{2}}$ contains the discrete forms of the advection, diffusion, and pressure gradient terms. Time and volume averaging equations (4) and (5) give

$$\langle\overline{\widehat{u}}\rangle_N = \langle\overline{u}^n\rangle_N + \Delta t\langle\overline{R}^{n+\frac{1}{2}}\rangle_N, \tag{6}$$

$$\langle\overline{u}^{n+1}\rangle_N = \langle\overline{\widehat{u}}\rangle_N + \Delta t\langle S^{n+\frac{1}{2}}\rangle_N. \tag{7}$$

To ensure no net acceleration of the flow, $\langle\overline{u}^{n+1}\rangle = u_0$ is imposed, where u_0 is the target volume-averaged velocity. Rearranging Eq. (7) then gives the evolution equation for $\langle S^{n+\frac{1}{2}}\rangle_N$ as

$$\langle S^{n+\frac{1}{2}}\rangle_N = \frac{1}{\Delta t}\left(u_0 - \langle\overline{\widehat{u}}\rangle_N\right). \tag{8}$$

The update for u^{n+1} [Eq. (5)] requires $S^{n+\frac{1}{2}}$ and not $\langle S^{n+\frac{1}{2}}\rangle_N$. Therefore, $S^{n+\frac{1}{2}}$ is extracted from the sum in Eq. (8), giving

$$\langle S^{n+\frac{1}{2}}\rangle_N = \frac{N-1}{N}\langle S^n\rangle_{N-1} + \frac{1}{N}S^{n+\frac{1}{2}}. \tag{9}$$

When combined with Eq. (8), $S^{n+\frac{1}{2}}$ is given by

$$S^{n+\frac{1}{2}} = \frac{N}{\Delta t}\left(u_0 - \langle\overline{\widehat{u}}\rangle_N\right) - (N-1)\langle S^n\rangle_{N-1}. \tag{10}$$

During the first few time steps when $n < N$, time averages must be taken over the previous n, rather than N, time steps.

Thus, $S^{n+\frac{1}{2}}$ is defined by the piecewise function

$$S^{n+\frac{1}{2}} = \begin{cases} \frac{N}{\Delta t}\left(u_0 - \langle\overline{\widehat{u}}\rangle_N\right) - (N-1)\langle S^n\rangle_{N-1} & n \geq N, \\ \frac{n}{\Delta t}\left(u_0 - \langle\overline{\widehat{u}}\rangle_n\right) - (n-1)\langle S^n\rangle_{n-1} & \text{otherwise.} \end{cases} \tag{11}$$

Equation (11) can be simplified if the time-averaging window is relaxed by letting $N = 1$. Under this simplification,

$$S^{n+\frac{1}{2}} = \frac{1}{\Delta t}\left(u_0 - \overline{\widehat{u}}\right). \tag{12}$$

The effect of various time-averaging windows on spin-up time was tested and had little effect on the method efficiency. We therefore choose $N = 1$ in what follows. We note that domains with fewer grid points or more complicated geometries (bed forms or steps) may benefit from extending the time-averaging window (i.e., $N > 1$) if the physical setup of the problem leads to a domain-averaged velocity that varies significantly over time scales that are long relative to the flow-through period.

The method is applied during model spin-up while turbulence evolves. As shown in the Appendix, we assume that the turbulence is developed when the total stress profile is approximately linear and

$$\frac{2\left(\langle\overline{P}\rangle - \langle\overline{\epsilon}\rangle\right)}{|\langle\overline{P}\rangle| + |\langle\overline{\epsilon}\rangle|} \leq r_k, \tag{13}$$

where $\langle\overline{P}\rangle$ and $\langle\overline{\epsilon}\rangle$ are the time- and volume-averaged production and dissipation, respectively. We refer to criterion (13) as the total kinetic energy (TKE) balance criterion, and note that, although the volume-integrated production and dissipation are in balance, they are locally balanced only in the equilibrium log layer. The time averaging is taken over one turnover period $T_\epsilon = H/u_*$, where $u_* = \sqrt{\overline{\tau}_B/H}$ is the friction velocity, and $\overline{\tau}_B$ is the planform-averaged bottom stress. Upon reaching statistical equilibrium based on criterion (13) with $r_k = 0.02$, we assume

$$S^{n+\frac{1}{2}} = S_T = \frac{u_*^2}{H}, \tag{14}$$

where S_T is the forcing required for a given friction Reynolds number once turbulence is statistically steady.

C. Overall solution procedure

The overall solution procedure is as follows:

1. Solve for $\widehat{u}$ using the Navier-Stokes code of choice with Eq. (4). $\widehat{u}$ will be the unforced update of u^n;
2. compute $\overline{\widehat{u}}$ and store for running average calculation in step 3;
3. compute $\langle\overline{\widehat{u}}\rangle_N$;
4. compute $S^{n+\frac{1}{2}}$ from Eq. (11) and store for running average calculation in step 6;
5. compute u^{n+1} from Eq. (5);
6. compute $\langle S^{n+\frac{1}{2}}\rangle_{N-1}$ for use in subsequent time step;
7. compute $\langle\overline{P}\rangle$ and $\langle\overline{\epsilon}\rangle$ (see the Appendix);
8. if the TKE balance criterion (13) is met, let $S^{n+\frac{1}{2}} = S_T$, otherwise repeat steps 1 through 7.

D. Computational details

We implement the method in the incompressible flow solver originally developed by Zang *et al.*[25] and later parallelized with the Message Passing Interface (MPI) by Cui.[26] The governing equations are discretized using a finite-volume method on a nonstaggered grid in general curvilinear coordinates. All spatial derivatives are discretized using second-order central differencing with the exception of advection, where a variation of QUICK (quadratic upstream interpolation for convective kinematics) is employed.[27] Time advancement of diagonal viscous terms is performed with the second-order accurate Crank-Nicolson method, whereas all remaining terms are advanced in time with the second-order accurate Adams-Bashforth method. The fractional step projection method[28] is used to enforce a divergence-free velocity field. Because the turbulence in our simulations is sufficiently resolved via the DNS approach, no subgrid-scale turbulence model is applied.

The computational domain is rectangular with streamwise, spanwise, and vertical dimensions of $7.5H \times 3.12H \times H$, discretized with $760 \times 320 \times 128$ cells. Grid spacing is constant in the horizontal, with $\Delta x^+ = \Delta y^+ = 4.88$. In the vertical, 5% grid stretching is applied, with a minimum Δz^+ at the bottom wall of 0.60. Grid stretching ceases at a height in which the vertical grid resolution is equal to the horizontal grid resolution. The momentum equations are evolved with a time step size that ensures a maximum Courant number of 0.4. Flow boundary conditions are periodic in the horizontal, free-slip at the top boundary ($\partial_z u = \partial_z v = 0$ and $w = 0$), and no-slip at the bottom boundary ($u = v = w = 0$). Following Moin and Kim,[3] two-point correlation functions confirm that the turbulent statistics are independent of the periodic boundary conditions. Simulations are run at the Army Research Laboratory DoD Supercomputing Resource Center (ARL DSRC) on Excalibur (Cray XC40) using 480 processors per simulation. On average, 1600 processor hours are required to simulate one turnover period.

E. Test cases

A total of 33 simulations are run, all initialized with $\overline{u} = u_0$ approximated by the volume average of a log-law velocity profile ($u_{\log} = u_*/\kappa \ln(z/z_0)$), which gives

$$u_0 = \frac{u_*}{\kappa}\left[\ln\left(\frac{H}{z_0}\right) + \frac{z_0}{H} - 1\right], \tag{15}$$

where κ is the von Kármán constant taken as 0.41, and $z_0 = \nu/(9u_*)$ is the smooth-wall bottom roughness. Velocity fields are initialized with either a log law (with a viscous sublayer from $z^+ = 0$ to 11.6) or linear mean profile, $\widetilde{u} = 2u_0 z/H$, plus a random field uniformly distributed over $[-\alpha u_0, \alpha u_0]$, where α is varied to test the effect of the initial perturbation magnitude. We note that it is difficult to determine u_0 exactly for a given Re_τ because of the existence of the wake and the transition zone between the viscous sublayer and the log law. Nevertheless, the approximate value is sufficiently close to the target, and as we will show, the true volume-averaged velocity is achieved soon after the TKE balance criterion is met.

TABLE I. Summary of runs performed.

Run	Re_τ	Initial profile	α	Forcing
R0	1	Linear	1.0	Eq. (11)
R1	500	Log law	1.0	Eq. (11) with the TKE criterion
R2	500	Log law	1.0	Constant S_T
R3a	500	Linear	1.0	Eq. (11) with the TKE criterion
R3b	400	Linear	1.0	Eq. (11) with the TKE criterion
R3c	300	Linear	1.0	Eq. (11) with the TKE criterion
R3d	200	Linear	1.0	Eq. (11) with the TKE criterion
R4a	500	Linear	1.0	Constant S_T
R4b	400	Linear	1.0	Constant S_T
R4c	300	Linear	1.0	Constant S_T
R4d	200	Linear	1.0	Constant S_T
R5-R15	500	Log law	0–1	Eq. (11) without the TKE criterion
R16-R26	500	Linear	0–1	Eq. (11) without the TKE criterion

Table I summarizes the initial conditions for all simulation runs. Run R0 ($Re_\tau = 1$) is simulated to show that the method produces the laminar, open-channel, Poiseuille flow solution when implemented for low Reynolds number flows. Runs R1, R2, R3a, and R4a ($Re_\tau = 500$) are compared in Sec. III A to illustrate differences between spin-up times using the method relative to equivalent simulations driven by a constant forcing ($S^{n+1/2} = S_T$). Applying $S^{n+\frac{1}{2}} = S_T$ is the same as forcing the flow with a constant pressure gradient. Runs R1 and R2 are computed for a total simulation time of $15T_\epsilon$ from identical initial conditions (log law plus random perturbations with $\alpha = 1$), but the method is implemented within R1, whereas R2 is driven by a constant forcing ($S^{n+1/2} = S_T$). The same is true for runs R3a and R4a, but initialization consists of a linear rather than a log-law mean velocity profile. In addition to runs R3a and R4a, runs R3b through R3d and runs R4b through R4d are simulated to confirm the method's validity for a range of Reynolds numbers (Re_τ varied from 200 to 500). Runs R5 through R26 are simulated for a total time of $10T_\epsilon$ to investigate the effects of initial conditions on flow development. In these runs, α varies from 0 to 1 in increments of 0.1, and the resulting perturbations are added to both log-law and linear initial velocity profiles. The purpose of runs R5 through R26 is to investigate flow development and the evolution of $S^{n+\frac{1}{2}}$. Accordingly, rather than imposing $S^{n+1/2} = S_T$ upon achieving the TKE balance criterion, these runs are forced with values of $S^{n+\frac{1}{2}}$ obtained from Eq. (11) throughout the simulations.

III. RESULTS AND DISCUSSION

A. Flow evolution

Methods for identifying statistical equilibrium of turbulent channel flow vary in the literature. Equilibrium is often identified by a time invariant mean velocity profile and a linear total stress profile.[3,4] Other definitions include the identification of a "quasi-periodic" total kinetic energy (TKE)[4] or time-invariant material derivatives of the Reynolds stresses.[20] Regardless of the definition of equilibrium, $\overline{u}$ must be constant in time when the flow is statistically steady. The time evolution of $\overline{u}$ during model spin-up is shown in Fig. 1(a) for runs R1, R2, R3a, and R4a. Because the method is implemented in runs R1 and R3a, the volume-averaged velocity is constant until the TKE balance criterion is met and $S^{n+1/2} = S_T$ is imposed. This switch occurs at $t = 10.4T_\epsilon$ for run R1 and $t = 4.6T_\epsilon$ for run R3a, as indicated in Fig. 1(a) by the black circle and cross, respectively. Once $S^{n+1/2} = S_T$ is imposed, the flow slightly accelerates because the target value of u_0 is slightly under predicted owing to the aforementioned lack of the viscous sublayer or wake in Eq. (15). The mean velocity and total stress profiles are steady by $t = 13.5T_\epsilon$ and $t = 10T_\epsilon$ for runs R1 and R3a, respectively.

The time evolution of $\overline{u}$ is different for simulations driven with a constant $S^{n+1/2} = S_T$ (runs R2 and R4a). In these cases, the flow accelerates during the early stage of spin-up [Fig. 1(a)]. This acceleration is explained by examining the forced, volume-averaged streamwise momentum equation for periodic open-channel flow with a free-slip top boundary, viz.,

$$\frac{\partial \overline{u}}{\partial t} = S_T - \frac{\widetilde{\tau_B}}{\rho_0 H} = S', \tag{16}$$

where ρ_0 is the fluid density, and $S' = S_T - \widetilde{\tau_B}/(H\rho_0)$. If $S' > 0$, the driving force exceeds the bottom stress and the flow accelerates. As shown in Figs. 1(a) and 1(b), positive values of S' correspond to periods of accelerating flow, and negative values correspond to decelerating flow for runs R2 and R4a. Because there is no imbalance between the bottom

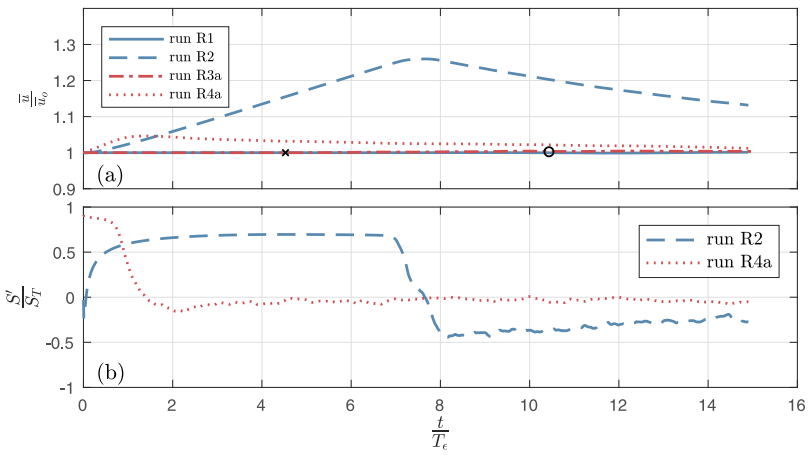

FIG. 1. (a) Time evolution of the volume-averaged streamwise velocity for runs R1, R2, R3a, and R4a, and (b) the bottom stress imbalance for runs R2 and R4a. The points in time at which the TKE balance criterion was met are indicated by the cross for run R1 ($t = 10.4T_\epsilon$) and circle for R3a ($t = 4.6T_\epsilon$).

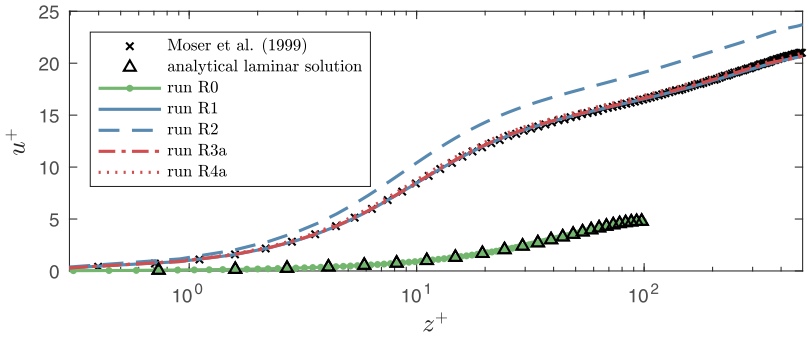

FIG. 2. Planform-averaged streamwise velocity profile runs R0, R1, R2, R3a, and R4a. Data from the work of Moser *et al.*[5] and the analytical solution to laminar, open-channel, Poiseuille flow are included for comparison.

stress and the forcing when the method is employed, $S' = 0$ and there is no acceleration of the volume-averaged velocity for runs R1 and R3a.

Sharp drops in S' in Fig. 1(b) indicate the onset of turbulence. Once transition to turbulence occurs, high momentum fluid mixes toward the lower wall, increasing velocity gradients and the associated bottom shear stress or flow resistance. As this occurs, S' decreases, eventually becoming negative, and the disproportionately high bottom stress decelerates the flow. The drop in S' occurs sooner for run R4a than it does for run R2, indicating the initial linear velocity profile transitions to turbulence faster than it does for the initial log-law profile. Because of the delayed transition, run R2 accelerates for a longer period before turbulence is triggered, leading to a larger velocity overshoot than run R4a.

Planform- and time-averaged streamwise velocity profiles ($u^+ = \langle\widetilde{u}\rangle/u_*$) for runs R0 through R4a are compared to results from the work of Moser *et al.*[5] ($Re_\tau = 590$) in Fig. 2. R0 ($Re_\tau = 1$) was evolved from a linear velocity profile for one viscous time scale (H^2/ν) to confirm that the method produces the laminar, open-channel, Poiseuille flow solution, $-\partial_x p(\frac{1}{2}z^2 - Hz)/\mu$. Here, μ is the dynamic viscosity. In Fig. 2, z was multiplied by 100 for run R0 for visualization purposes. The resulting streamwise velocity profile is virtually indistinguishable from the analytical solution. For runs R1, R2, R3a, and R4a, time averages were taken over the last two turnover periods ($2T_\epsilon$). Runs R1 and R2 overlap and closely match the work of Moser *et al.* except near the top boundary. We apply a free-slip boundary condition at the top, whereas Moser *et al.* applied no-slip boundary conditions to the top and bottom boundaries in a domain with a channel height that is twice the channel height in our simulations. We only compare our results to those over half of the channel in the work of Moser *et al.*

The velocity overshoot for run R2 (constant forcing with log-law initialization) is evident in Fig. 2. Run R4a (constant forcing with linear initialization) also overshoots but to a lesser extent. As indicated in Fig. 1, both flows are decelerating and will eventually reach the same profiles as runs R1 and R3a. However, the deceleration is slow. Based on the decay indicated in Fig. 1(a), we expect run R2 to achieve the correct velocity profile after roughly $t = 65T_\epsilon$ and run R4a after roughly $t = 41T_\epsilon$. This implies that with constant forcing run R2 takes 4.8 times longer than run R1, and run R4a takes 4.1 times longer than run R3a. Since the simulations require roughly 1600 CPU hours for each turnover period, this translates into 82 400 more CPU hours for run R2 over run R1 and 49 600 more CPU hours for run R4a over run R3a.

The statistically steady state of runs R1 and R3a is confirmed by overlapping Reynolds stress profiles. Root-mean-square velocity fluctuations $\sqrt{\widetilde{u'_\alpha u'_\alpha}}$ (Greek indices imply no summation), and the vertical Reynolds stress component, $-\widetilde{u'w'}$, are shown in Fig. 3. The profiles for run R3a overlap those for run R1 in all four panels. Owing to the velocity overshoot, the magnitude of all Reynolds stress components for run R2 is larger than those for the equilibrium profiles given by runs R1 and R3a. The same is true of run R4a, with the exception of $\sqrt{\widetilde{v'v'}}$. Runs R2 and R4a have not converged to a statistically steady state.

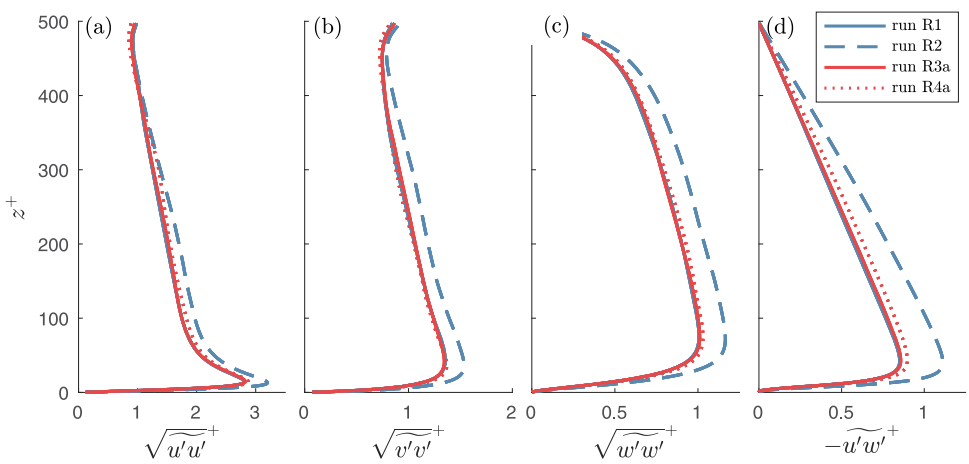

FIG. 3. Profiles of root-mean-square velocity fluctuations in the (a) streamwise, (b) spanwise, and (c) vertical directions, and (d) the vertical Reynolds stress component. Runs R1 and R3a overlap in all plots.

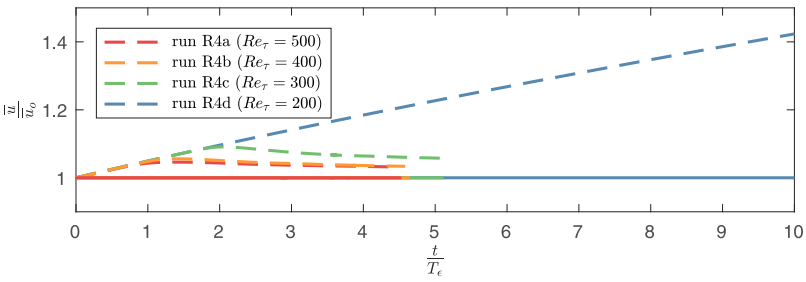

FIG. 4. Time evolution of the volume-averaged streamwise velocity for runs R3a through R3d and runs R4a through R4d. Results are plotted for each case up to the point when the TKE balance criterion is met. The color coding for runs R3a through R3d is the same as for R4a through R4d, but R3 simulations correspond to solid lines.

Before the onset of turbulence, the flow behaves as laminar Poiseuille flow. The larger the ratio between the laminar to turbulent $\overline{u}$ for a given pressure gradient, the faster the flow accelerates. This ratio depends on Re_τ and is given by

$$\frac{(\overline{u})_{\text{laminar}}}{(\overline{u})_{\text{turbulent}}} = \frac{\kappa Re_\tau}{3}\left[\ln\left(9Re_\tau\right) + \frac{1}{9Re_\tau} - 1\right]^{-1} \sim \frac{Re_\tau}{\ln(Re_\tau)}. \tag{17}$$

Therefore, increasing Re_τ causes a larger initial acceleration. This dependency on Re_τ is evident in Fig. 4, where the time evolution of $\overline{u}$ is shown for runs R3a through R3d (Re_τ 200 though 500 forced with the method) and runs R4a through R4d (Re_τ 200 through 500 with constant forcing). The color coding for the R3 runs is the same as the R4 runs, but the R3 runs are represented by solid lines. All simulations presented in Fig. 4 are initialized with a linear velocity profile plus random perturbations with $\alpha = 1$. $\overline{u}$ is plotted for each simulation pair, for example, R3a and R4a, up until the point in time at which the TKE balance criterion is met for the simulation forced with the method (R3a for the example pair). The initial slopes of the R4 runs are similar, yet time is normalized by T_ϵ, which implies that higher Re_τ simulations accelerate faster than lower Re_τ simulations (T_ϵ is smaller for larger Re_τ). The inflection points for lower Re_τ runs occur later in time because the onset of turbulence is delayed with decreasing Re_τ for a given initial velocity profile and perturbation magnitude. The delay is caused by a reduction in the mean shear stress as will be discussed in Sec. III D. The large overshoot for run R4d illustrates that enforcing no net acceleration of the flow is more important when the onset of turbulence is delayed. Since run R4d does not transition to turbulence, the flow continuously accelerates throughout the simulation.

B. Connection between forcing function and bottom stress

Because $S^{n+\frac{1}{2}}$ ensures a time-invariant $\overline{u}$ over N steps, $\langle S\rangle_N$ is expected to exactly balance the discrete, time- and planform-averaged bottom shear stress, $\langle\widetilde{\tau_B}^{n+\frac{1}{2}}\rangle_N$. This is shown by first combining Eqs. (6) and (7) to give

$$\langle\overline{u}^{n+1}\rangle_N = \langle\overline{u}^{n}\rangle_N + \Delta t\langle\overline{R}^{n+\frac{1}{2}}\rangle_N + \Delta t\langle S^{n+\frac{1}{2}}\rangle_N. \tag{18}$$

Recognizing the method ensures $\langle\overline{u}^{n+1}\rangle_N = \langle\overline{u}^{n}\rangle_N = u_0$; Eq. (18) reduces to

$$\langle S^{n+\frac{1}{2}}\rangle_N = -\langle\overline{R}^{n+\frac{1}{2}}\rangle_N, \tag{19}$$

where $R^{n+\frac{1}{2}}$ in Cartesian coordinates is given by

$$R^{n+\frac{1}{2}} = \frac{\partial}{\partial x_j}\left(-u_j^n u^n + \nu\frac{\partial u}{\partial x_j}^{n+\frac{1}{2}}\right) - \frac{1}{\rho_0}\frac{\partial p}{\partial x}^{n+\frac{1}{2}}, \tag{20}$$

where $p^{n+\frac{1}{2}}$ is the pressure, j = 1, 2, 3, and the Einstein summation convention is assumed. Although the method is implemented in curvilinear coordinates, we present the derivation in Cartesian coordinates for simplicity. Taking the discrete volume average of Eq. (20) over a rectangular domain gives

$$\begin{aligned}\overline{R}^{n+\frac{1}{2}} &= \frac{1}{V}\sum_x\sum_y\sum_z R^{n+\frac{1}{2}}\\ &= \frac{1}{V}\sum_x\sum_y\sum_z\left[\frac{\partial}{\partial x_j}\left(-u_j^n u^n + \nu\frac{\partial u}{\partial x_j}^{n+\frac{1}{2}}\right) - \frac{1}{\rho_0}\frac{\partial p}{\partial x}^{n+\frac{1}{2}}\right]\\ &= \frac{1}{V}\sum_x\sum_y\left(-w^n u^n + \nu\frac{\partial u}{\partial z}^{n+\frac{1}{2}}\right)_{\text{T}}\\ &\quad - \frac{1}{V}\sum_x\sum_y\left(-w^n u^n + \nu\frac{\partial u^{n+\frac{1}{2}}}{\partial z}\right)_{\text{B}},\end{aligned} \tag{21}$$

where $w = u_3$, and the T and B subscripts correspond to the top and bottom boundaries, respectively. We move from the volume integration to the surface integration in Eq. (21) by applying the discrete form of Gauss' theorem. Terms containing fluxes and the pressure gradient evaluated at sidewalls are eliminated in Eq. (21) due to horizontal periodicity. Assuming no flow through the top and bottom boundaries, $w_T = w_B = 0$, and a free-slip top condition, $\partial_z u = \partial_z v = 0$, gives

$$\overline{R}^{n+\frac{1}{2}} = -\frac{1}{V}\sum_x\sum_y\left(\nu\frac{\partial u}{\partial z}^{n+\frac{1}{2}}\right)_B. \tag{22}$$

Denoting the viscous bottom stress as

$$\tau_B^{n+\frac{1}{2}} = \rho_0\left(\nu\frac{\partial u}{\partial z}^{n+\frac{1}{2}}\right)_B, \tag{23}$$

combining Eqs. (19) and (22) gives

$$\begin{aligned}\langle S^{n+\frac{1}{2}}\rangle_N &= \left\langle\frac{1}{\rho_0 V}\sum_x\sum_y\tau_B^{n+\frac{1}{2}}\right\rangle_N\\ &= \left\langle\frac{1}{\rho_0 H}\left(\frac{1}{A}\sum_x\sum_y\tau_B^{n+\frac{1}{2}}\right)\right\rangle_N\\ &= \frac{1}{\rho_0 H}\langle\widetilde{\tau_B}^{n+\frac{1}{2}}\rangle_N,\end{aligned} \tag{24}$$

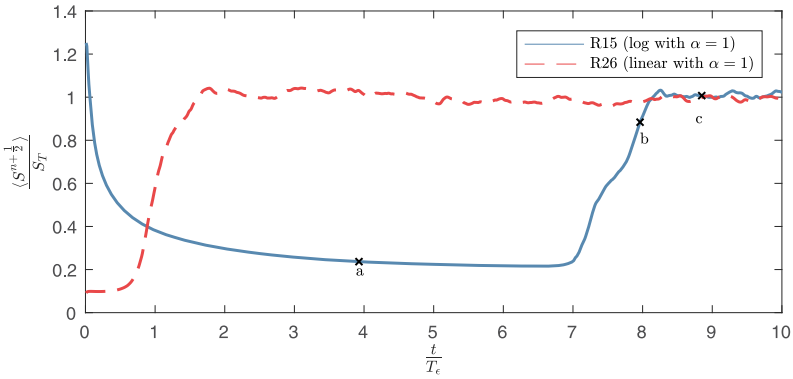

FIG. 5. Time evolution of $\langle S^{n+\frac{1}{2}} \rangle$ normalized by S_T for runs 15 (initial log law with $\alpha = 1$) and 26 (initial linear profile with $\alpha = 1$). Letters indicate the contour plot times shown in Fig. 6.

where the domain volume is $V = AH$. Eq. (24) shows that $\langle S^{n+\frac{1}{2}} \rangle_N$ is the driving force that exactly balances the time- and planform-averaged viscous bottom stress over N time steps.

The time evolution of $\left\langle S^{n+1/2} \right\rangle$ (or just $S^{n+1/2}$ since $N = 1$) is plotted for runs R15 (initial log law with $\alpha = 1$) and R26 (initial linear profile with $\alpha = 1$) in Fig. 5. These simulations are forced with $S^{n+\frac{1}{2}}$ defined by Eq. (11) for their entirety (i.e., without setting $S^{n+\frac{1}{2}} = S_T$ when the TKE balance criterion is met) to study the behavior of the forcing function itself. Normalizing $\langle S^{n+1} \rangle$ by S_T ensures values near 1 indicate turbulent flow. Over the first $7T_\epsilon$ for run R15, the forcing exponentially decays as the initial log-law profile (which has relatively high bottom shear stress) is smoothed by viscous diffusion until reaching a parabolic profile (which has relatively low bottom shear stress). This transition to Poiseuille flow occurs because the laminar flow lacks turbulent vertical momentum fluxes required to sustain the log-law profile. The resulting lower near-wall velocity gradients lead to a reduction in the bottom stress and hence the value of $\left\langle S^{n+1/2} \right\rangle$.

Instantaneous velocity magnitude contoured over a streamwise plane is shown in Fig. 6 to illustrate flow evolution. The time corresponding to each panel is indicated by letters in Fig. 5. Figure 6(a) is a representative of the flow before the onset of turbulence. As the simulation progresses, disturbances develop near the bottom and initiate three-dimensional flow structures shown in Fig. 6(b). $\langle S^{n+\frac{1}{2}} \rangle$ then increases to balance the increasing bottom shear stress as turbulent fluxes vertically mix momentum over a time scale of roughly one turnover period (from approximately $7 < T_\epsilon < 8$ for R15 and $0.6 < T_\epsilon < 1.6$ for R26 in Fig. 5). The log-law profile is attained in the time-averaged sense. Figure 6(c) is representative of the flow after it has become fully turbulent. Flow evolution for run R26 is similar to run R15, with one notable difference. Because run R26 is initialized with a linear velocity profile, the initial bottom shear stress is small and is not significantly affected by viscous diffusion. As a result, $\langle S^{n+\frac{1}{2}} \rangle$ is nearly constant until the transition to turbulence.

C. Global turbulence production and dissipation

Volume average turbulent kinetic energy production ($\overline{P}$) and dissipation ($\overline{\epsilon}$) are computed at each time step from the discrete evolution equation for the volume average turbulent kinetic energy, $\overline{k} = 0.5\overline{u_i' u_i'}$ (see the Appendix for derivation). As shown in the Appendix, the exact discrete time rate of change of the volume-averaged TKE is given by $(\overline{k}^{n+1} - \overline{k}^{n})/\Delta t = \overline{P} - \overline{\epsilon}$.

Time series of the TKE budget terms and the volume-averaged TKE are shown in Fig. 7 for run R1. During the early part of run R1 ($0 \le t < 7T_\epsilon$), production and dissipation are negligible. However, $\overline{k}$ steadily increases as instabilities develop and eventually lead to turbulence ($t \approx 7T_\epsilon$). Production and subsequently dissipation increase rapidly, although the growth of $\overline{\epsilon}$ lags slightly behind that of $\overline{P}$. During transition to turbulence ($7T_\epsilon < t < 8T_\epsilon$), production exceeds dissipation, causing the TKE to grow beyond its equilibrium value, followed by a decay over the next three turnover periods when dissipation exceeds production. Beyond $t \approx 11T_\epsilon$ (when the TKE balance criterion is met), production and dissipation are roughly in balance, leading to a negligible $(\overline{k}^{n+1} - \overline{k}^{n})/\Delta t$.

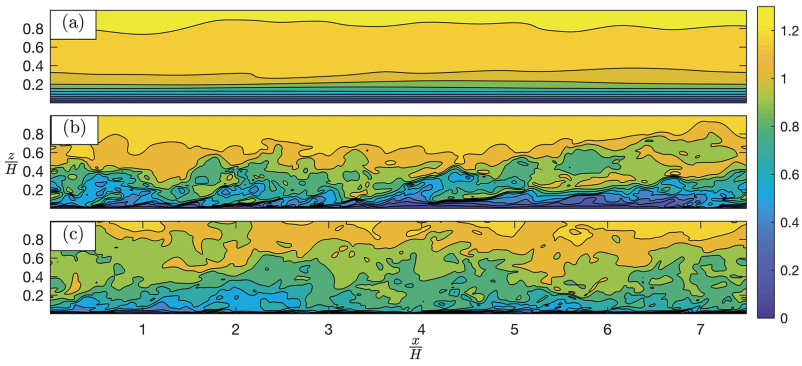

FIG. 6. Normalized velocity magnitude $[(u^2 + v^2 + w^2)^{1/2}/u_0]$ along the channel centerline at different flow development stages for run 15. The time corresponding to each panel is indicated in Fig. 5.

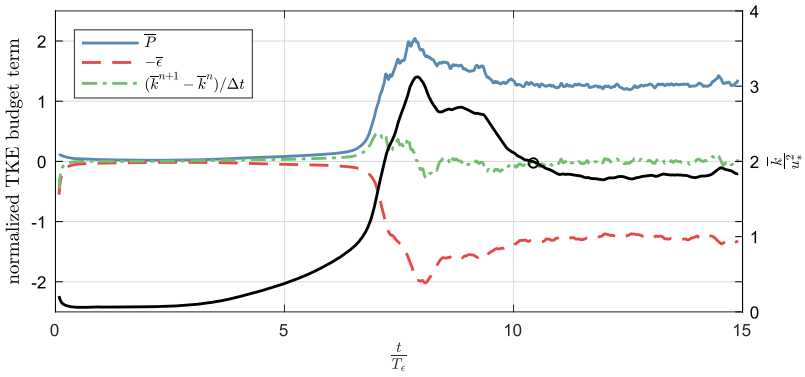

FIG. 7. Time evolution of $\overline{P}$, $-\overline{\epsilon}$, and $(\overline{k}^{n+1}-\overline{k}^{n})/\Delta t$ (left vertical axis) and instantaneous $\overline{k}$ (right vertical axis) for run R1. The black circle indicates the point in time at which the TKE balance criterion is met. All budget terms are normalized by $A_\epsilon u_*^3/H$, where $A_\epsilon = 6.2$ (see the Appendix).

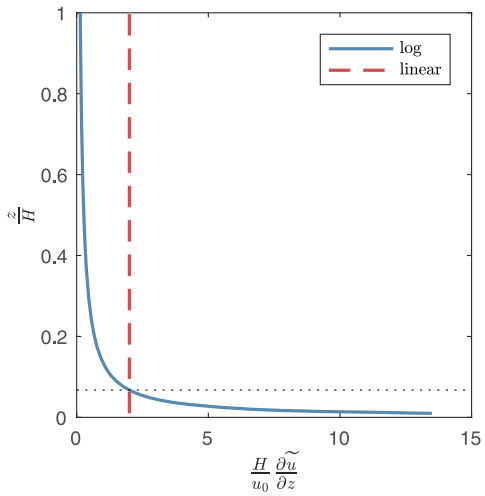

FIG. 8. Nondimensional vertical shear for a log law and a linear velocity profile, demonstrating how the constant shear for the linear profile exceeds that for the log law over 93% of the domain (above dotted line).

D. Effect of initial conditions

With the exception of the bottom 7% of the channel, the mean shear for a linear velocity profile is greater than that for a log-law profile with $Re_\tau = 500$ when both have the same volume-averaged velocity (Fig. 8). Therefore, because production of TKE is a function of the mean velocity shear, runs initialized with a linear mean velocity profile transition to turbulence sooner than those initialized with a log law. The uniform shear over the channel for the linear profile generates turbulence within $t = 10T_\epsilon$ throughout the domain when initializing simulations with $\alpha \geq 0.3$. However, for simulations initialized with a log law, transition to turbulence occurs much later in time and only after instabilities develop in the strongly sheared, near-wall region.

We define the normalized volume-averaged mean kinetic energy as

$$\gamma = \frac{\overline{\widetilde{u_i}\widetilde{u_i}} - \overline{u_{\log}^2}}{\overline{u_{\log}^2}} \tag{25}$$

to quantify the departure of the simulated mean velocity profiles from a log-law distribution. For a log-law velocity profile, γ is close to but not identically zero because of the viscous sublayer and wake. For a linear mean velocity profile, $\gamma = 0.29$ when $Re_\tau = 500$. As shown in Fig. 9, before the onset of turbulence, the velocity profile approaches the laminar parabolic velocity profile (for which $\gamma = 0.17$) regardless of the initial condition. As a result, the value of γ increases for simulations initialized with a log law and decreases for simulations initialized with a linear profile. However, after transition to turbulence, $\gamma \to 0$ for all simulations because they approach the log law.

The magnitude of the initial perturbation given by α affects the onset of turbulence since production also depends on the velocity fluctuations. Simulations initialized with larger perturbations transition to turbulence sooner, as indicated by the drop in the value of γ which occurs earlier in time for increasing values of α in Fig. 9. In order for turbulence to develop over the period simulated ($10T_\epsilon$) with an initial linear velocity profile, $\alpha \geq 0.3$. However, owing to the weak shear away from the bottom, turbulence only develops when $\alpha = 1.0$ when the flow is initialized with a log law. Instabilities begin to develop toward the end of the simulation when $\alpha = 0.9$

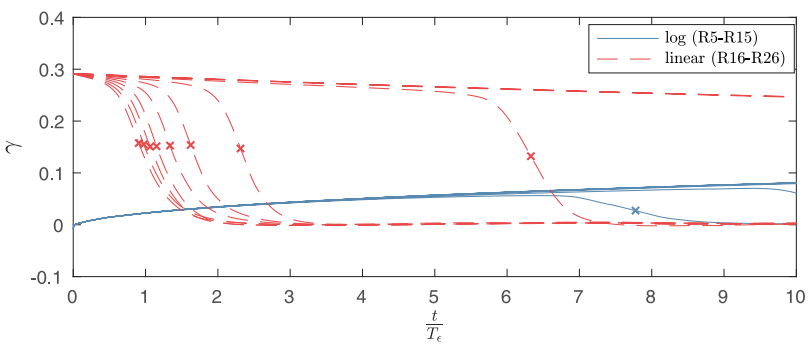

FIG. 9. Time evolution of γ, a measure of the departure from the log-law velocity profile, for different values of the initial perturbation, α, with initial linear (runs R5-R15) and log-law (runs R6-R26) profiles. The crosses indicate inflection points in γ to quantify the turbulent transition time, T_t. For the linear initial profile, the flow transitions for values of $\alpha = 0.3, 0.4, 0.5, \ldots, 1.0$, with the transition time becoming smaller for increasing α. The flow transitions for the initial log-law profile only when $\alpha = 1.0$.

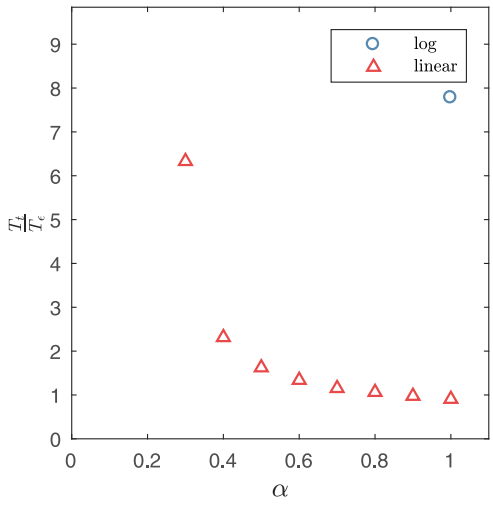

FIG. 10. Effect of the initial perturbation magnitude, α, on the turbulent transition time, T_t, for initial linear and log-law velocity profiles.

for the log-law initialization, although the flow does not have time to transition (Fig. 9). Smaller values of α would eventually lead to transition at later times, but this would incur significant computational cost. We note that simulations with initial perturbations drawn from a Gaussian distribution were also tested (not shown), although the difference in turbulence transition times compared to a uniform distribution with the same variance was negligible.

To quantify the time required for the onset of turbulence, we define the turbulent transition time, T_t, as the time of the inflection point in γ (denoted by crosses in Fig. 9), which corresponds to the zero crossing of the second time derivative of γ. This transition time is plotted against α in Fig. 10 for runs R5 through R26. Simulations that do not transition to turbulence are omitted. For simulations initialized with a linear velocity profile, the turbulence transition time exponentially decays with increasing α, asymptotically approaching one eddy turnover period. The eddy turnover period physically represents the time required for the largest turbulent motions to vertically mix momentum over the channel height and hence is the expected minimum amount of time needed for transition to turbulence. Because of the exponential behavior, smaller values of the initial perturbations significantly delay transition. However, increasing α does not lead to monotonic decrease in the computation time because of the constraint on the time step size to ensure numerical stability for large initial perturbations.

IV. SUMMARY AND CONCLUSIONS

We developed a method to ensure a constant volume-averaged streamwise velocity during spin-up of turbulent channel or open-channel flow. The method computes a streamwise force that exactly balances the bottom stress at each time step, thus preventing flow acceleration. Without our method, simulations imposing the target force accelerate beyond the target velocity, resulting in a significant increase in computational time required for the flow to become statistically steady as the volume-averaged velocity slowly decays to the target.

Although the method guarantees a constant volume-averaged velocity, the time to reach statistical equilibrium is highly dependent on the initial velocity profile and perturbation magnitudes. The initial velocity profile affects the time required to reach equilibrium because it sets the mean shear contributing to the production of TKE. At the same time, the magnitude of the initial perturbations also contributes to TKE production by altering the Reynolds stresses. We find that initialization with a linear mean velocity profile leads to statistically steady turbulence faster in time than initialization with a log-law velocity profile. This time reduction occurs because the vertical shear in a log law is confined to the near-wall region, whereas it is constant and larger over more than 93% of the domain for a linear profile with the same average velocity. When the magnitude of the perturbations is smaller than $\alpha = 1$, simulations initialized with a log law do not transition to turbulence in less than 10 turnover periods for $Re_\tau = 500$. However, simulations initialized with a linear profile transition to turbulence for perturbations as small as $\alpha = 0.3$, although the time to reach equilibrium asymptotically approaches one turnover period with increasing perturbation magnitude. Therefore, there is no optimum α that minimizes the time to reach equilibrium, and large values of α can impact numerical stability through the Courant number restriction. Our results imply a good balance is achieved with a value of $\alpha = 0.7$ for $Re_\tau = 500$, which does not impact stability and transitions the flow to turbulence in 1.2 turnover periods when initialized with a linear velocity profile. Although other initial velocity profiles might further accelerate transition to turbulence, it is unlikely that transition would occur in less than one turnover period.

Given that a simulation driven with a constant force and initialized with a log law and 100% perturbations could take over 65 turnover periods to reach statistical equilibrium, the results in this paper suggest that the simulation time can be reduced by a factor of 6.5 when employing our method, since the same simulation initialization with a linear velocity profile and $\alpha = 0.7$ is statistically steady after just 10 turnover periods. We note that any method ensuring a constant volume-averaged or bulk velocity will result in a similar spin-up reduction time, given the same initial conditions. Although these findings were obtained with $Re_\tau = 500$, the time to reach equilibrium could be longer with larger Re_τ when driving the flow with a constant forcing because flow acceleration increases with increasing Re_τ. However, our method guarantees that the volume-averaged velocity is constant independent of Re_τ.

Although we focused on ensuring a constant volume-averaged velocity, the method can also be implemented in a way that ensures a constant planform-averaged bottom stress by imposing a force that ensures a desired planform-averaged velocity for the first grid cell above the wall. However, during flow spin-up, the lack of the correct Reynolds stresses needed to balance the force outside of the viscous sublayer would lead to significant acceleration of the volume-averaged velocity. Turbulence would likely develop quickly in this case due to the strong near-wall shear, but significant computational time would be needed for the volume-averaged flow to decelerate to the target. Therefore, it is more appropriate to enforce a constant volume-averaged velocity than a constant bottom stress.

Our method can be applied to open-channel flow with a variable bottom, although the force that is computed to maintain a constant volume-averaged velocity would be one that balances both the viscous stress and form drag. Both of these forces are automatically accounted for in the method regardless of the shape of the wall or the Reynolds number. Since the force by the wall in such a case is typically not known *a priori*, the only option would be to impose a force that ensures a constant volume-averaged velocity, rather than a force that imposes a constant planform-averaged bottom stress.

ACKNOWLEDGMENTS

K.S.N. gratefully acknowledges the Charles H. Leavell Graduate Student Fellowship. K.S.N. and O.B.F. acknowledge the Stanford Woods Institute for the Environment and Office of Naval Research (ONR) Grant No. N00014-15-1-2287.

APPENDIX: DISCRETE TKE EVOLUTION EQUATION

Local production and dissipation of TKE can be computed from spatial discretizations of

$$P = \widetilde{u_i' u_j'} \frac{\partial \widetilde{u}_i}{\partial x_j}, \tag{A1}$$

$$\epsilon = \nu \widetilde{\frac{\partial u_i'}{\partial x_j} \frac{\partial u_i'}{\partial x_j}}, \tag{A2}$$

where everything under the tilde is planform-averaged. However, statistical equilibrium is not necessarily indicated by $\langle \overline{P} \rangle = \langle \overline{\epsilon} \rangle$ when calculating $\overline{P}$ and $\overline{\epsilon}$ from volume-averaged, discrete approximations of Eqs. (A1) and (A2) due to numerical errors. While these errors are small, we find it important to compute an exact discrete evolution equation for the TKE in order to ensure the TKE balance criterion.

The exact discrete evolution equation for the TKE is derived by first combining Eqs. (4) and (5) and expanding $R^{n+\frac{1}{2}}$ into its individual terms. For the time advancement scheme employed by Zang *et al.*,[25] this gives

$$\frac{u_i^{n+1} - u_i^n}{\Delta t} = \frac{3}{2} C\left(u_i^n\right) - \frac{1}{2} C\left(u_i^{n-1}\right) + G_i\left(p^{n+\frac{1}{2}}\right) + \frac{1}{2} D\left(u_i^{n+1} + u_i^n\right) + S^{n+\frac{1}{2}}, \tag{A3}$$

where C, G, and D are the discrete operators for advection, the pressure gradient, and diffusion, respectively. The discrete form of the evolution equation for u_i' is found by subtracting the planform average of Eq. (A3) from itself to obtain

$$\frac{u'^{n+1}_i - u'^{n}_i}{\Delta t} = \frac{3}{2}\left(C\left(u_i^n\right) - \widetilde{C}\left(u_i^n\right)\right) - \frac{1}{2}\left(C\left(u_i^{n-1}\right) - \widetilde{C}\left(u_i^{n-1}\right)\right) + G_i\left(p'^{n+\frac{1}{2}}\right) + \frac{1}{2} D\left(u'^{n+1}_i + u'^{n}_i\right). \tag{A4}$$

The discrete evolution equation for the TKE is then found by multiplying Eq. (A4) by $1/2[(u')_i^{n+1} + (u')_i^n]$, giving

$$\frac{k^{n+1} - k^n}{\Delta t} = \frac{1}{2}(u'^{n+1}_i + u'^{n}_i)\left[\frac{3}{2}\left(C\left(u_i^n\right) - \widetilde{C}\left(u_i^n\right)\right) - \frac{1}{2}\left(C\left(u_i^{n-1}\right) - \widetilde{C}\left(u_i^{n-1}\right)\right)\right] + \frac{1}{2}(u'^{n+1}_i + u'^{n}_i)\left[G_i\left(p'^{n+\frac{1}{2}}\right) + \frac{1}{2} D\left(u'^{n+1}_i + u'^{n}_i\right)\right]. \tag{A5}$$

In the continuous sense, the term containing the discrete diffusion operator D in Eq. (A5) is responsible for both diffusion and dissipation of TKE. However, volume averaging eliminates the diffusion because there is no diffusive flux of TKE at the boundaries. Therefore, the volume average of the diffusion term in Eq. (A5) equals the volume-averaged dissipation, viz.,

$$\overline{\epsilon} = \overline{\frac{1}{4}(u'^{n+1}_i + u'^{n}_i) D\left(u'^{n+1}_i + u'^{n}_i\right)}. \tag{A6}$$

Following similar arguments, the volume average of the advection operators in Eq. (A5) gives the volume-averaged production of TKE, viz.,

$$\overline{P} = \overline{\frac{1}{4}(u'^{n+1}_i + u'^{n}_i)\left[3\left(C\left(u_i^n\right) - \widetilde{C}\left(u_i^n\right)\right) - \left(C\left(u_i^{n-1}\right) - \widetilde{C}\left(u_i^{n-1}\right)\right)\right]}, \tag{A7}$$

so that the discrete evolution of the volume-averaged TKE is given by $(\overline{k}^{n+1} - \overline{k}^n)/\Delta t = \overline{P} - \overline{\epsilon}$. Time averaging over one turnover period ($N_\epsilon = T_\epsilon/\Delta t$ time steps) gives $(\overline{k}^{n+1} - \overline{k}^{n-N_\epsilon+2})/T_\epsilon = \langle \overline{P} \rangle - \langle \overline{\epsilon} \rangle$. The TKE balance criterion then implies

$$2\frac{\overline{k}^{n+1} - \overline{k}^{n-N_\epsilon+2}}{T_\epsilon\left(|\langle \overline{P} \rangle| + |\langle \overline{\epsilon} \rangle|\right)} = 2\frac{\langle \overline{P} \rangle - \langle \overline{\epsilon} \rangle}{\left(|\langle \overline{P} \rangle| + |\langle \overline{\epsilon} \rangle|\right)} \le r_k, \tag{A8}$$

where $r_k \ll 1$. During equilibrium, we can assume $\langle \overline{P} \rangle = \langle \overline{\epsilon} \rangle = A_\epsilon u_*^3/H$, where the constant is given approximately by

$$A_\epsilon = \frac{1}{\kappa}\left[\ln\left(\frac{Re_\tau}{z^+_{\text{ref}}}\right) - \frac{1}{\kappa z^+_{\text{ref}}} - 1\right], \tag{A9}$$

where we have assumed $z^+_{\text{ref}} \ll Re_\tau$ and z^+_{ref} is a reference height introduced by vertical averaging. Eq. (A9) is derived by assuming a log-law mean velocity profile and a linear Reynolds stress distribution with height (with a correction in the viscous

sublayer, following Ref. 29) and vertically averaging over z_{ref} to H (z^+_{ref} to Re_τ). Choosing $z^+_{\text{ref}} = 11.6$, which is where the theoretical velocity profiles in the viscous sublayer and log law intersect, and $Re_\tau = 500$ gives $A_\epsilon = 6.2$. Substitution gives the simplified TKE balance criterion,

$$\overline{k}^{n+1} - \overline{k}^{n-N+2} \leq r_k A_\epsilon u_*^2. \tag{A10}$$

Therefore, employing the exact discrete forms of the production and dissipation terms in Eqs. (A6) and (A7), we guarantee that the volume-averaged TKE change over one turnover period is small, and the maximum change based on Eq. (A10) is much smaller than $A_\epsilon u_*^2$.

[1] J. W. Deardorff, "A numerical study of three-dimensional turbulent channel flow at large Reynolds numbers," J. Fluid Mech. **41**, 453–480 (1970).
[2] U. Schumann, "Subgrid scale model for finite difference simulations of turbulent flows in plane channels and annuli," J. Comput. Phys. **18**, 376–404 (1975).
[3] P. Moin and J. Kim, "Numerical investigation of turbulent channel flow," J. Fluid Mech. **118**, 341–377 (1982).
[4] J. Kim, P. Moin, and R. Moser, "Turbulence statistics in fully developed channel flow at low Reynolds number," J. Fluid Mech. **177**, 133–166 (1987).
[5] R. D. Moser, J. Kim, and N. N. Mansour, "Direct numerical simulation of turbulent channel flow up to $Re_\tau = 590$," Phys. Fluids **11**, 943–945 (1999).
[6] J. C. Del Alamo, J. Jiménez, P. Zandonade, and R. D. Moser, "Scaling of the energy spectra of turbulent channels," J. Fluid Mech. **500**, 135–144 (2004).
[7] S. Hoyas and J. Jiménez, "Scaling of the velocity fluctuations in turbulent channels up to $Re_\tau = 2003$," Phys. Fluids **18**, 011702 (2006).
[8] X. Wu and P. Moin, "A direct numerical simulation study on the mean velocity characteristics in turbulent pipe flow," J. Fluid Mech. **608**, 81–112 (2008).
[9] M. Bernardini, S. Pirozzoli, and P. Orlandi, "Velocity statistics in turbulent channel flow up to $Re_\tau = 400$," J. Fluid Mech. **742**, 171–191 (2014).
[10] A. Lozano-Durán and J. Jiménez, "Effect of the computational domain on direct simulations of turbulent channels up to $Re_\tau = 4200$," Phys. Fluids **26**, 011702 (2014).
[11] H. Choi, P. Moin, and J. Kim, "Direct numerical simulation of turbulent flow over riblets," J. Fluid Mech. **255**, 503–539 (1993).
[12] P. Cherukat, Y. Na, T. Hanratty, and J. McLaughlin, "Direct numerical simulation of a fully developed turbulent flow over a wavy wall," Theor. Comput. Fluid Dyn. **11**, 109–134 (1998).
[13] V. De Angelis, P. Lombardi, and S. Banerjee, "Direct numerical simulation of turbulent flow over a wavy wall," Phys. Fluids **9**, 2429–2442 (1997).
[14] R. P. Garg, J. H. Ferziger, S. G. Monismith, and J. R. Koseff, "Stably stratified turbulent channel flows. I. Stratification regimes and turbulence suppression mechanism," Phys. Fluids **12**, 2569–2594 (2000).
[15] V. Armenio and S. Sarkar, "An investigation of stably stratified turbulent channel flow using large-eddy simulation," J. Fluid Mech. **459**, 1–42 (2002).
[16] M. I. Cantero, S. Balachandar, A. Cantelli, C. Pirmez, and G. Parker, "Turbidity current with a roof: Direct numerical simulation of self-stratified turbulent channel flow driven by suspended sediment," J. Geophys. Res. **114**, 1–20, doi:10.1029/2008jc004978 (2009).
[17] J. Kim and P. Moin, "Large eddy simulation of turbulent channel flow: ILLIAC 4 calculation," in *Turbulent Bourdary Layers- Experiments, Theory, and Modeling, The Hague, The Netherlands, AGARD Conference Proceedings* (1979), Vol. 271, available at https://ntrs.nasa.gov/search.jsp?R=19790023981.
[18] M. Lee, R. Ulerich, N. Malaya, and R. D. Moser, "Experiences from leadership computing in simulations of turbulent fluid flows," Comput. Sci. Eng. **16**, 24–31 (2014).
[19] Y.-J. Chou and O. B. Fringer, "Modeling dilute sediment suspension using large-eddy simulation with a dynamic mixed model," Phys. Fluids **20**, 115103 (2008).
[20] M. Lee and R. D. Moser, "Direct numerical simulation of turbulent channel flow up to $Re_\tau = 5200$," J. Fluid Mech. **774**, 395–415 (2015).
[21] J. Fröhlich, *Large Eddy Simulation Turbulenter Strömungen* (Springer, 2006), Vol. 1.
[22] S. Koltakov, "Bathymetry inference from free-surface flow features using large-eddy simulation," Ph.D. thesis, Stanford University, 2013.
[23] T. Kempe, "A numerical method for interface-resolving simulations of particle-laden flows with collisions," Ph.D. thesis, Technische Universität, Dresden, 2011.
[24] M. Quadrio, B. Frohnapfel, and Y. Hasegawa, "Does the choice of the forcing term affect flow statistics in DNS of turbulent channel flow?," Eur. J. Mech. B-Fluid. **55**, 286–293 (2016).
[25] Y. Zang, R. L. Street, and J. R. Koseff, "A non-staggered grid, fractional step method for time-dependent incompressible Navier-Stokes equations in curvilinear coordinates," J. Comput. Phys. **114**, 18–33 (1994).
[26] A. Cui, "On the parallel computation of turbulent rotating stratified flows," Ph.D. thesis, Stanford University, Stanford, CA, USA, 1999.
[27] B. Leonard, "A stable and accurate convective modelling procedure based on quadratic upstream interpolation," Comput. Methods Appl. Mech. Eng. **19**, 59–98 (1979).
[28] J. Kim and P. Moin, "Application of a fractional-step method to incompressible Navier-Stokes equations," J. Comput. Phys. **59**, 308–323 (1985).
[29] S. B. Pope, *Turbulent Flows* (Cambridge University Press, 2000).